Catalytic Dephosphorylation Using Ceria Nanocrystals

Michael J. Manto, Pengfei Xie, Chao Wang[*]

Department of Chemical and Biomolecular Engineering, Johns Hopkins University, Baltimore, Maryland 21218, United States

KEYWORDS: *dephosphorylation, heterogeneous catalysis, ceria nanocrystals, phosphorus*

Abstract. Phosphorus is a crucial element for living systems and plays significant roles in plant growth. The world's supply of phosphorus today however relies on depleting feedstocks such as phosphate rocks, while the demand for phosphorus fertilizers escalates as the population continues to grow. It is thus urgent to develop sustainable sources and production methods for phosphorus. Here we report on catalytic dephosphorylation for recovery of phosphates from organic and biological molecules. Ceria (CeO_2) nanocrystals were synthesized with shape control and applied as "artificial phosphatases" to cleave the phosphate ester bond in *para*-nitrophenyl phosphate (*p*-NPP) and release free phosphate anions in aqueous solutions. The dephosphorylation reaction was studied on the CeO_2 nanocrystals at various temperatures to evaluate the dependences of rate constant, activation energy and recyclability on the particle shape. The structure-property relationship established in these studies suggests that the oxygen vacancies on the surface of CeO_2 are the active sites for dephosphorylation.

INTRODUCTION

As an essential element in living systems, phosphorus is crucial for cell division and growth, energy storage and conversion, respiration, photosynthesis, and other biological processes.[1] Phosphorus is found naturally in soil, but concentrations can fall down to very low levels depending on geographic conditions, and artificial phosphorus fertilizers are demanded to sustain the growth of crops.[2-3] Before the early 1900s, most of the world's phosphorus was derived from animal wastes. Today the vast majority (nearly 80%) of phosphorus in fertilizers comes from phosphate rocks, which are primarily harvested in the remote Western Sahara region.[4] It is predicted that the production of phosphate rocks will reach its peak before 2040 and the reserves will be completely depleted by the end of this century.[5-6] It thus becomes imperative to develop innovative and sustainable methods for production of phosphorus from renewable sources.

One solution toward this sustainability challenge is to extract phosphorus from phosphorylated biomolecules (e.g., phospholipids and nucleic acids[7]) and recycle it for fertilizer production. This is conventionally done via fermentation,[8-9] which produces struvite, a precipitate that can be processed to make phosphorus fertilizers.[10-11] Alternatively, a more robust approach is catalytic dephosphorylation. By hydrolytic cleavage of the phosphate ester bond, free phosphate anions can be released from biomass and agriculture wastes, which can then be captured and regenerated as chemical streams for further applications.[12-13] Previously studies of cerium oxide (CeO_2) nanocrystals for biological applications (e.g., cancer therapy[14-15], pharmacology[16-17] and toxin mitigation[18]) have shown that these nanomaterials can function as artificial phosphatases and catalyze the dephosphorylation of nucleic acids, peptides, DNA and RNA under ambient conditions.[19-22] Thereby CeO_2 is believed to be a promising catalyst for dephosphorylation and recovery of phosphorus from biomass and organic wastes.

Despite the great potential, very little is known about the catalytic mechanism of CeO_2 for the dephosphorylation reaction. In this work, we used *para*-nitrophenyl phosphate (*p*-NPP) as a model molecule to perform kinetic studies of the dephosphorylation reaction on CeO_2 nanocrystals (Scheme 1). CeO_2 nanocrystals were synthesized by NaOH-mediated hydrothermal growth with the shape controlled by altering the reaction temperature and/or introducing hexamethylenetetramine (HMT) as a surfactant. Pseudospherical, octahedral, cubic, and rod-like CeO_2 nanocrystals were obtained and subjected to catalytic studies for dephosphorylation in aqueous solutions at temperatures ranging from 5°C to 95°C. Yields of phosphate and *para*-nitrophenol (*p*-NP), rate constants, activation energies and recyclability were systematically evaluated for the CeO_2 nanocrystals of different shapes. The dependence of reaction kinetics on the surface structures are discussed to depict the active sites on these catalysts.

RESULTS AND DISCUSSION

Synthesis and Characterization of CeO_2 Nanocrystals. Figure 1(a-h) shows the TEM and HRTEM images of the as-synthesized CeO_2 nanocrystals of different morphologies. The CeO_2 nanospheres have an average diameter of 4 nm (Figure 1(a)). Although the lattice fringes exhibited in the HRTEM images (Figure 1(e)) can be ascribed to (111) planes (with an inter-plane spacing of 0.32 nm) of CeO_2 in the fluorite phase, the CeO_2 nanospheres have no preferential exposure of a certain facet on the surface. The CeO_2 nanooctahedra have a size of ~18 nm with (111) facet preferentially exposed on the surface (Figure 1(b, f)). The CeO_2 nanorods have a diameter of 10 nm on average, with the length varying from 50 to 150 nm (Figure 1(c)). It can be seen from the HRTEM images that the CeO_2 nanorods possess a polycrystalline nature, likely with (100) and (110) facets (with inter-plane distances of 0.19 nm and 0.28 nm, respectively) preferentially exposed on the sidewalls (Figure 1(g)). The CeO_2 nanocubes have a rather wide distribution of particle size, with the edge length varying from 20 to 120 nm, and the surface is dominated by (100) facets (Figure 1(d, h)). Figure 1(i) presents the XRD patterns collected for the CeO_2 nanocrystals, in comparison to commercial CeO_2 nanopowders (see the Supporting Information for TEM images, Figure S5). The major peaks at 28.5°, 33.1°, 47.5°, and 56.3° can be assigned to the (111), (200), (220), and (311) planes of CeO_2 adopting the fluorite structure (space group $Fm\bar{3}m$, JCDPS No. 65-2795). Among the nanocrystals of different shapes, CeO_2 nanorods exhibit lower peak intensities, indicating poorer crystallinity than the others, which is consistent with the observations from HRTEM images. A summary of the average particle sizes determined from TEM images and the specific surface areas measured by BET analysis is presented in Table 1.

It has been reported that oxygen vacancies are usually present in CeO_2 nanocrystals, which are associated with Ce^{3+} and can be characterized by XPS.[23-26] Figure 1(j) shows the Ce 3d XPS spectra collected for the CeO_2 nanocrystals. The spectra exhibit two multiplets (denoted as v and u) that correspond to the $3d_{5/2}$ and $3d_{3/2}$ core holes of Ce and have a spin-orbit splitting of ~18.6 eV. All the peaks in the spectra for octahedral and cubic nanocrystals can be ascribed to $Ce^{(4+)}O_2$, with each multiplet comprised of three peaks and a total of six peaks assigned to three different energy states: u (904 eV) and v (886 eV) for $Ce(3d^9 4f^2)$-$O(2p^4)$, u^{II} (911 eV) and v^{II} (893 eV) for $Ce(3d^9 4f^1)$-$O(2p^5)$, and u^{III} (920 eV) and v^{III} (902 eV) for $Ce(3d^9 4f^0)$-$O(2p^6)$. For nanorods and nanospheres, four additional peaks are present in the spectra, which are believed to be associated with Ce^{3+}: u^0 (901 eV) and v^0 (884 eV) for $Ce(3d^9 4f^1)$-$O(2p^6)$, and u^I (907 eV) and v^I (889 eV) for $Ce(3d^9 4f^2)$-$O(2p^5)$. Stronger Ce^{3+} peaks were observed for the CeO_2 nanorods and nanospheres than for the cubic and octahedral nanocrystals. This could correspond to the presence of more oxygen vacancies on the former two types of nanocrystals, considering the formation energy of oxygen vacancy follows the trend (110) < (100) < (111) for the various low-index facets of CeO_2.[27-29] It is however necessary to point out that this correlation may be undermined by the potential presence of impurity phases (such as Ce_2O_3) in small amounts and that the probing of Ce^{3+} by XPS is not surface-specific for the CeO_2 nanocrystals.

Catalytic Studies and Kinetics of Dephosphorylation. The CeO_2 nanocrystals of different shapes were applied as catalysts for dephosphorylation of *para*-nitrophenyl phosphate (*p*-NPP) in aqueous solutions. *p*-NPP is a common chromogenic substrate used in enzyme-linked immunosorbent assay (ELISA) and spectrophotometric analysis of phosphatases.[30-32] Both *p*-NPP and its hydrolysis product, *p*-NP (converted into *para*-nitrophenolate after the pH adjustment, see the Experimental Methods), exhibit distinct optical absorption properties, making it possible to track the reaction progress by using spectroscopic means. Meanwhile, the produced phosphate can be analyzed by using the molybdenum blue assay (see the Experimental Method). The concentrations of *p*-NPP, *p*-NP and phosphate can thus be determined by comparing against the corresponding standard solutions (Figure S6).

Figure 2(a) shows the UV-Vis spectra collected over the course of dephosphorylation of *p*-NPP on CeO_2 nanooctahedra at 25°C. The peak corresponding to *p*-NPP near 310 nm dissipated as the reaction proceeded, accompanied with the gradual increase of peak intensity for *p*-NP near 405 nm, indicating the conversion of *p*-NPP to *p*-NP. Figures 2(b) summarizes the concentrations of *p*-NPP, *p*-NP and phosphate depending on the reaction time. It can be seen that the conversion of *p*-NPP to *p*-NP and phosphate was nearly stoichiometric, indicating that no undesirable side reactions or competing products were involved in the dephosphorylation process.

The CeO_2 nanocrystals of different shapes had substantially different performances in the dephosphorylation of *p*-NPP. Figure 2(c) shows the comparisons of time-dependent reaction yields among the various types of CeO_2 nanocrystals at 25°C. The nanospheres and nanooctahedra delivered much higher yields of *p*-NP and phosphate than the nanocubes and nanorods. After 8 h of reaction, the yield of *p*-NP reached 82.0 ± 5.0%, 90.5 ± 3.6%, 82.0 ± 5.0%, 23.0 ± 3.8%, and 4.7 ± 2.5% for the nanospheres, nanooctahedra, nanorods, and nanocubes, respectively. Similar trends were also observed in the yield of phosphate (Figure 2(d)). It is noteworthy that the yields of phosphate were consistent with the yields of *p*-NP for the different types of CeO_2 nanocrystals, suggesting the complete desorption of phosphate from the catalyst surface. Besides changing with reaction time, the reaction yields were also found to be dependent on the temperature (Figure 2(e)). For all the CeO_2 nanocrystals, higher yields were observed as the reaction temperature increased, reaching ~90% after 8 h at 95°C. In the temperature range of 5 – 65°C, nanospheres and nanooctahedra outperformed the nanocubes and nanorods.

Figure 3 summarizes the results of kinetic analysis for the various types of CeO_2 nanocrystals. The dephosphorylation of *p*-NPP was found to be first order with respect to *p*-NPP (Figure 3(a)). For nanooctahedra, the rate constants were measured to be 0.011 ± 0.001, 0.24 ± 0.06, 1.1 ± 0.4, 5.0 ± 0.5, 25 ± 2 and 39 ± 2 h^{-1} at 5°C, 25°C, 50°C, 65°C, 80°C and 95°C, respectively. Rate constants normalized by catalyst loading (k_m, Figure 3(b)) and specific surface area (k_s, Figure 3(c)) for the CeO_2 nanocrystals of different shapes follows the trend: nanosphere > nanooctahedra > nanorod > nanocube. The most active nanospheres had a k_m value of 331 ± 29 g^{-1} h^{-1} and k_s of 2.3 ± 0.2 m^{-2} h^{-1}. The increase of rate constant with temperature indicates a positive value of the apparent activation energy, as seen from the Arrhenius plots for the various CeO_2 catalysts presented in Figure 3(d). The activation energy was found to be 36.6 ± 1.2 kJ/mol, 76.5 ± 1.9 kJ/mol, 82.0 ± 3.6 kJ/mol, and 105.4 ± 2.9 kJ/mol for the nanospheres, nanooctahedra, nanorods, and nanocubes, respectively, in comparison to 57.4 ± 2.7 kJ/mol for the commercial

CeO_2 catalyst (Figure 3(e)). The trend of activation energy correlates inversely to that for TOF, highlighting the structure sensitivity of the dephosphorylation reaction on CeO_2.

Active Sites on CeO_2 Catalysts. From above it can be seen that the catalytic activity for dephosphorylation is highly dependent on the shape of the CeO_2 nanocrystals. The catalytic activity follows the order: nanospheres > nanooctahedra > nanorods > nanocubes, whereas the trend for activation energy is inversed. Considering the preferential exposure of (111) on the nanooctahedra, (110) and (100) on the nanorods and (100) on the nanocubes, it is suggested that the catalytic activity for dephosphorylation of the different low-index facets of CeO_2 follows the trend: (111) > (110) > (100). This dependence could be correlated to the Lewis acidity of the surface Ce^{4+} cations, which can coordinate phosphoryl oxygen and activate the dissociation of the P−O bond.[33] It is however noticed that the correlation between surface structures and acid-base properties of CeO_2 facets is still under debate in the literature. It has been believed that the acidity of Ce^{4+} on ordered, defect-free surfaces follows the order (100) > (110) > (111),[34] but this trend is obviously opposite to and cannot explain the observed dependence of dephosphorylation catalytic activity on the shape of CeO_2 nanocrystals.[22] Meanwhile, it is noticed that spectroscopic investigations on CeO_2 nanocrystals show weak dependence of acidity on the nanocrystal shape and surface facets.[35] While the different conclusions could be either a result of the intrinsically complex structure-property relationship of this reducible oxide or simply caused by the dissimilar synthetic methods in the various studies, it becomes difficult to draw explicit connections between the dephosphorylation catalytic performance and the Lewis acidity of Ce^{4+} cations for the CeO_2 nanocrystals.

Besides Ce^{4+} on the ordered facets, the XPS analysis has shown the presence of Ce^{3+} in the CeO_2 nanospheres and nanorods (Figure 1(j)). It is reported that surface Ce^{3+} sites could play an important role in the dephosphorylation reaction considering the biomimetic functionality of binuclear Ce(III)-Ce(IV) complex.[21] As Ce^{3+} is usually associated with the formation of oxygen vacancy,[29] whereas the formation energy of vacancy varies among the different facets of CeO_2, it is plausible that the dependence of catalytic activity on the particle shape is a result of the different surface densities of oxygen vacancy. Studies of temperature-programmed desorption of oxygen (O_2-TPD) was thus performed for quantitative analysis of the oxygen vacancies on the surface of the CeO_2 nanocrystals.[36-37]

Figure 4(a, b) presents the patterns for temperature-programmed desorption of oxygen (O_2-TPD) recorded on the various types of CeO_2 nanocrystals. Two desorption peaks are observed in these profiles: the first one at 150 – 210°C, which can be assigned to adsorbed molecular oxygen (ad-O_2) on oxygen vacancies, and the second one at 400 – 460°C corresponding to atomic oxygen evolved from the bulk of CeO_2. Surface density of oxygen vacancy estimated based on the amounts of ad-O_2 follows the order: nanospheres > commercial > nanooctahedra ≈ nanorods > nanocubes (Figure 4(c)). This trend correlates well to the dependence of activation energy on the particle shape, namely decreasing E_a with increasing surface density of oxygen vacancies. Moreover, the turnover frequency (TOF) derived from normalization of the rate constant with the surface density of oxygen vacancies was found to increase as the surface vacancy density increases, reaching $827 \pm 46\ h^{-1}$ for the most active nanospheres. These findings indicate that the active sites for dephosphorylation on CeO_2 are associated with the oxygen vacancies, with the surface density of oxygen vacancies being a good descriptor for the reaction kinetics. The catalytic mechanisms associated with oxygen vacancies are thus speculated to involve activation of the phosphoryl ester molecules at acid-base pair centers such as Ce^{3+}-O, □-O (□ denotes an oxygen vacancy site), or □-OH (hydroxyl group adsorbed on nearby Ce cation sites).[38-41] It is further noted that the onset temperature for oxygen desorption follows a similar trend as the surface density of oxygen vacancy, with the nanospheres having the lowest onset temperature (Figure 4b). This finding indicates that the nanospheres have the weakest binding to ad-O_2, which may also facilitate the desorption of dephosphorylation products (phosphate and/or *p*-NP).

Catalyst Recyclability. Recyclability represents an important merit of catalysts in practical applications. Figure 5 summarizes the evolution of *p*-NP yield during five subsequent runs of dephosphorylation reaction (8 h for each run). It was found that the yield of *p*-NP had a significant drop for the nanooctahedra and nanorods, whereas the loss of catalytic activity for the nanospheres was almost negligible. At the end of the recyclability test, approximately 1%, 7% and 10% drop in yield of *p*-NP was observed for the nanospheres, nanooctahedra and nanorods, respectively, as compared to 7% for the commercial CeO_2. The yield of *p*-NP from the CeO_2 nanocubes was consistently low and never exceeded ~5% throughout the recyclability studies.

From TEM images collected for the CeO_2 nanocrystals after the tests, it can be seen that the difference in recyclability is well correlated to the extents of particle aggregation (Figure 5(b-f)). The nanorods and nanocubes had the most severe aggregation, followed by the nanooctahedra and commercial CeO_2, whereas the nanospheres exhibited negligible aggregation. These results are in line with the consensus of size- and shape-dependent colloidal assembly and stability of nanocrystals.[42-44]

CONCLUSION

We have performed systematic studies of catalytic dephosphorylation using CeO_2 nanocrystals. CeO_2 nanocrystals of different shapes were synthesized and demonstrated as “artificial phosphatases” to cleave the phosphate ester bond in *para*-nitrophenyl phosphate (*p*-NPP) and release free phosphate anions. The dephosphorylation reaction kinetics, including rate constant and activation energy, as well as the catalyst recyclability, were found to be dependent on the particle shape and surface defects, with the catalytic activity following the trend nanosphere > nanooctahedra > nanorod > nanocube. By correlating the reaction kinetics to the surface structure analysis based on O_2-TPD, the active sites for dephosphorylation were demonstrated to be associated with oxygen vacancies on the surface of the CeO_2 nanocrystals. Our work highlights the potential of catalytic dephosphorylation for recovery of phosphorus nutrients from biomass and organic wastes.

METHODS

Materials and Chemicals. The following chemicals were purchased and used as-received without further purification: cerium(IV) oxide (nanopowder, $\geq$ 99.5%, Alfa Aesar), cerium(III) nitrate hexahydrate ($Ce(NO_3)_3$-$6H_2O$, 99% trace metals basis, Aldrich), hexamethylenetetramine ($(CH_2)_6N_4$, HMT, $\geq$ 99%, Aldrich), hydrogen peroxide (H_2O_2, ACS grade, 30 wt%, Fisher), sodium hydroxide (NaOH, 99.1%, Fisher), *para*-nitrophenol ($C_6H_5NO_3$, *p*-NP, $\geq$ 99%, Aldrich), *para*-nitrophenyl phosphate disodium salt hexahydrate ($C_6H_4NO_6PNa_2$-$6H_2O$, *p*-NPP, $\geq$ 99%, Sigma), L-ascorbic acid ($C_6H_8O_6$, reagent grade, Sigma), ammonium molybdate tetrahydrate ($(NH_4)_6Mo_7O_{24}$-$4H_2O$, ACS reagent, 81.0-83.0% MoO_3 basis, Sigma-Aldrich), sodium phosphate dibasic (Na_2HPO_4, $\geq$ 98.5%, Sigma), sulfuric acid (H_2SO_4, ACS grade, BDH), and anhydrous ethanol (C_2H_5OH, 200 proof, ACS/USP grade, Pharmco-Aaper). Deionized water was collected from an ELGA PURELAB flex apparatus.

Synthesis of CeO_2 Nanocrystals. For the synthesis of CeO_2 nanospheres, 1 mmol of cerium nitrate hexahydrate ($Ce(NO_3)_3 \cdot 6H_2O$) and 32 mL of 0.078 M NaOH were added to a 100 mL reaction flask. The mixture was stirred at 700 rpm for 22 h at 25°C in air. The CeO_2 nanospheres were collected and washed with ethanol and deionized water three times by centrifugation at 10,000*g* for 10 min and were dispersed in deionized water for further use.

For the synthesis of CeO_2 nanooctahedra, a 100 mL reaction flask was charged with 5 mL of 0.0375 M $Ce(NO_3)_3$, 1 mL of 0.5 M hexamethylenetetramine (HMT), and an additional 5 mL of deionized water. The mixture was stirred at 700 rpm in air and heated to 75°C for 3 h. The solution slowly turned from clear to turbid white, indicating the formation of CeO_2 nanocrystals. The precipitated CeO_2 nanooctahedra were annealed in static air at 200°C for 12 h to remove the HMT surfactant.

Similar to the synthesis of nanospheres, CeO_2 nanorods were synthesized by mixing 5 mL of 0.4 M $Ce(NO_3)_3$ and 35 mL of 9 M NaOH in a Teflon-lined stainless steel autoclave, and then heating this mixture at 100°C for 24 h. CeO_2 nanocubes were made by a similar approach to the nanorods with 5 mL of 1.5 M $Ce(NO_3)_3$ and 35 mL of 6 M NaOH.

Material Characterization. Transmission electron microscopy (TEM) images were taken on an FEI Tecnai 12 operating at 100 kV. High-resolution transmission electron microscopy (HRTEM) images were captured on a Phillips CM 300 FEG operating at 300 kV. TEM samples were prepared by dispersing the CeO_2 nanocrystals in ethanol and depositing droplets of the obtained solution on Cu grids (400 mesh, coated with carbon film), with the solvent evaporated under ambient conditions. X-ray diffraction (XRD) patterns were obtained from a PANalytical X'Pert^3 X-ray diffractometer equipped with a Cu Kα radiation source (λ = 1.5406 Å). X-ray photoelectron spectroscopy (XPS) measurements were taken on a PHI 5400 X-ray photoelectron spectrometer equipped with an Al Kα X-ray source. Nitrogen adsorption measurements were measured on dried powders of CeO_2 nanocrystals using a Micromeritics ASAP 2020, with the nanocrystals degassed under vacuum for 8 h at 180°C and measured at a temperature ramping rate of 5°C/min. Specific surface areas (SSA) were calculated according to the Brunauer-Emmett-Teller (BET) theory.

Catalytic Studies. A stock solution of *p*-NPP was first prepared at a concentration of 0.2 mg/mL. An aliquot (10 mL) of this stock solution was mixed with 3.5 mg of CeO_2 nanocrystals which was then heated to the desired reaction temperature (ranging from 3 to 95°C) using an ice bath or a hot plate. The reaction was carried out under ambient conditions. As the reaction proceeded, the solutions turned from turbid white to turbid yellow, indicating the formation of *para*-nitrophenol (*p*-NP). At different time intervals, 0.5 mL of the reaction solution was collected, to which 0.5 mL of ethanol was added. After removing the CeO_2 catalyst by centrifugation (16,000 rpm for 5 min), the collected solution was further treated with NaOH (1 %) to adjust the pH and convert *para*-nitrophenol to *para*-nitrophenolate.[45] Ultraviolet-visible absorption spectra were collected by using a SpectraMax Plus 384 spectrometer to analyze the concentrations of *p*-NPP and *p*-NP.

The concentration of phosphate produced from the dephosphorylation reaction was characterized by using a modified molybdenum blue assay (see more details in the Supporting Information).[46-47] A stock solution of 0.088 mg/mL of sodium phosphate was first prepared, and then diluted in a series (0.5 dilution factor) to create the standards for calibration. 200 µL of the assay was used for 1 mL of reaction solution or phosphate standard. UV-Vis absorption was measured at 890 nm and the absorbance was used to analyze the concentration of phosphorus.

In performing the recyclability studies, the same catalyst loading and reaction concentration was maintained. After each run of dephosphorylation reaction for 8 h, the catalyst was isolated from the reaction mixture by centrifugation and re-dispersed in deionized water by sonication, which was then added to a fresh *p*-NPP solution for the next run.

Temperature-Programmed Desorption of Oxygen (O_2-TPD). O_2-TPD patterns were collected on CeO_2 nanocrystal powders (ca. 100 mg) using a gas chromatograph (GC-2010 Plus equipped with a Barrier Ionization Discharge (BID) detector, Shimadzu). Dried catalysts were loaded in a plug flow reactor with a quartz tube of 1/8" in diameter, and pretreated in He at 300°C for 1 h. After cooled down to room temperature, oxygen adsorption was performed by flowing O_2 (20 mL/min) for 30 min. The physically adsorbed oxygen was removed by purging with He for ~60 min. For desorption, the temperature was increased from room temperature to 600°C at a ramping rate of 5°C/min. The desorbed oxygen was carried out by a flow of He (20 mL/min) and analyzed by the GC-BID.

ASSOCIATED CONTENT

Supporting Information. More experimental details, characterizations and kinetic results. This material is available free of charge via the Internet at http://pubs.acs.org

AUTHOR INFORMATION

Corresponding Author

*Email: chaowang@jhu.edu

Author Contributions

The manuscript was written through contributions of all authors. All authors have given approval to the final version for submission.

Notes

The authors declare no competing financial interest.

ACKNOWLEDGMENT

This work is supported by the National Science Foundation (CBET-1437219) and the Johns Hopkins Catalyst Award. We thank Michael Barclay (JHU) for the help on collecting XPS spectra, Dr. Kenneth Livi (JHU) for HRTEM imaging, and Yanran Cui (Purdue) for BET analysis.

Scheme 1. Illustration of the catalytic dephosphorylation of *p*-NPP.

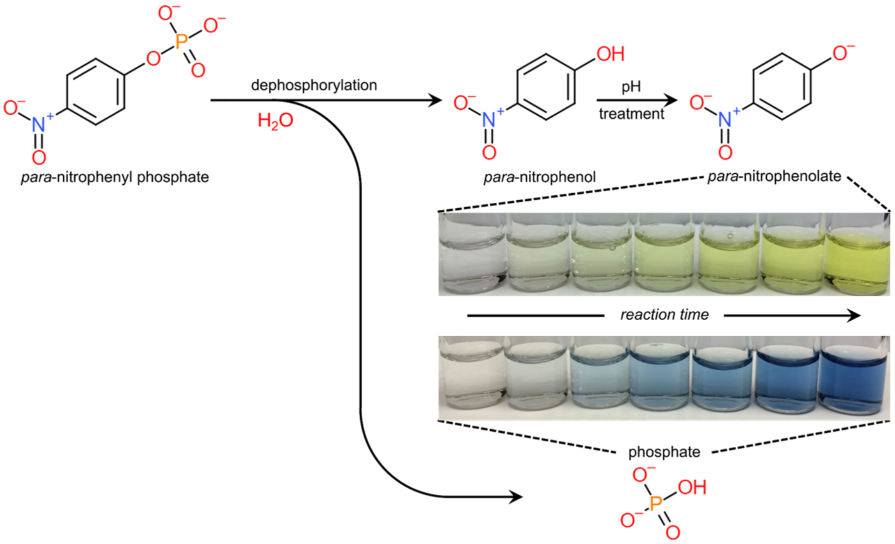

Table 1. Summary of surface facets, particle sizes, and BET surface areas for the CeO_2 nanocrystals.

CeO_2 Nanocrystals	Exposed Crystal Facets	Size Distribution from TEM (nm)	BET Surface Area (m^2/g)
Nanospheres	*	4.0 ± 0.6	142.7
Nanooctahedra	(111)	18.0 ± 1.6	69.8
Nanorods	(100) (110)	10 ± 3 (width) 91 ± 36 (length)	66.2
Nanocubes	(100)	72 ± 50	8.0
Commercial	*	16 ± 4	71.6

*No explicit surface facets were found for the nanospheres and commercial catalyst.

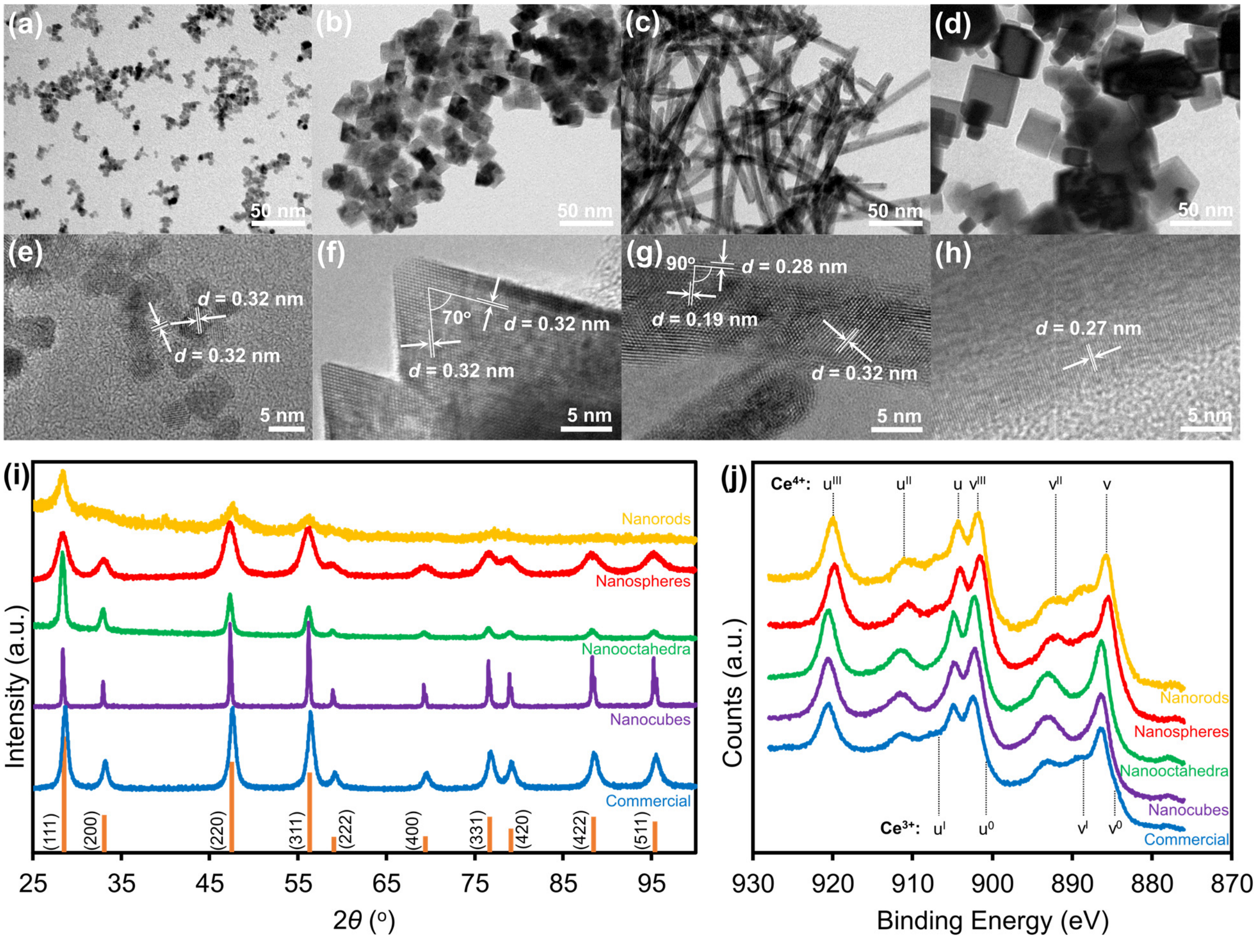

Figure 1. TEM and HRTEM images of the (a, e) CeO_2 nanospheres, (b, f) CeO_2 nanooctahedra, (c, g) CeO_2 nanorods, and (d, h) CeO_2 nanocubes, respectively. (i) XRD patterns of the CeO_2 nanocrystals indexed to JCDPS No. 65-2795 for CeO_2 with a fluorite type of crystal structure. (j) Ce $3d_{2/3,5/2}$ XPS spectra of the CeO_2 nanocrystals. Characteristic peaks for Ce^{3+} correspond to the following energy states: u^0 and v^0 for $Ce(3d^94f^1)$-$O(2p^6)$ and u^I and v^I for $Ce(3d^94f^2)$-$O(2p^5)$. Characteristic peaks for Ce^{4+} correspond to the following energy states: u and v for $Ce(3d^94f^2)$-O $(2p^4)$, u^{II} and v^{II} for $Ce(3d^94f^1)$-$O(2p^5)$, and u^{III} and v^{III} for $Ce(3d^94f^0)$-$O(2p^6)$.

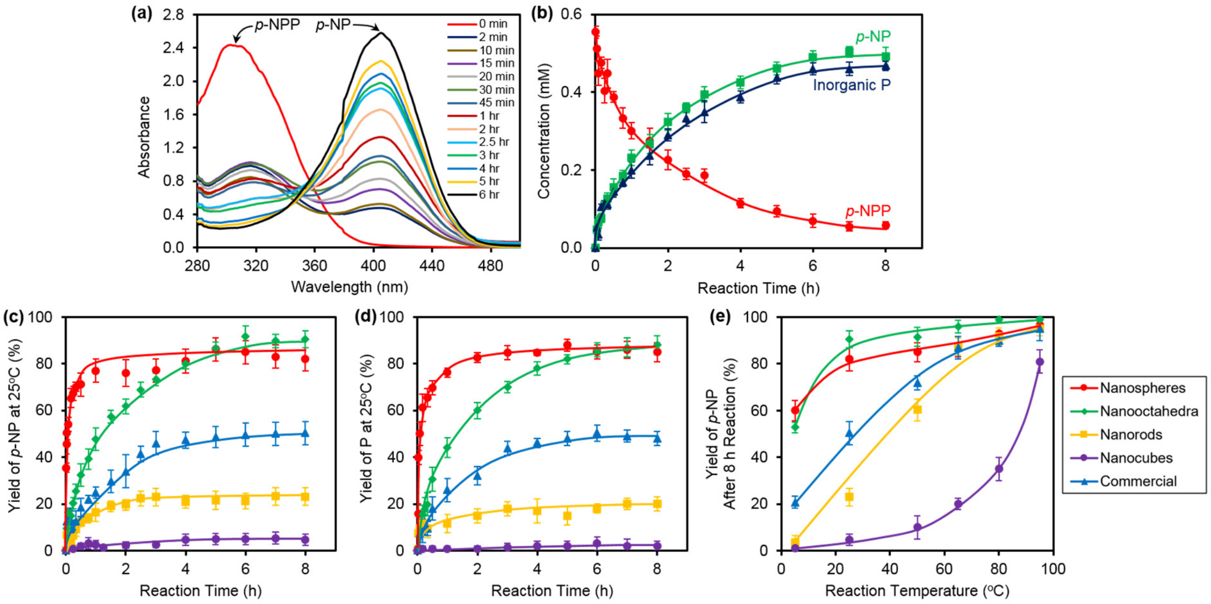

Figure 2. (a) UV-Vis spectra for reaction supernatants collected at selected time intervals. The reaction in this sample spectra was catalyzed by CeO_2 nanooctahedra at 25°C. The characteristic absorption peak occurs near 310 nm for *p*-NPP and near 410 nm for *p*-NP after pH adjustment. (b) Time-dependent concentration profiles of *p*-NPP, *p*-NP and phosphorus determined for dephosphorylation over CeO_2 nanooctahedra at 25°C. Tim-dependent yields of (c) *p*-NP and (d) phosphorus at 25°C for each CeO_2 catalyst. (e) Yields of *p*-NP after 8 h of reaction at various temperatures. Color coding for (c – e) is presented on the right side.

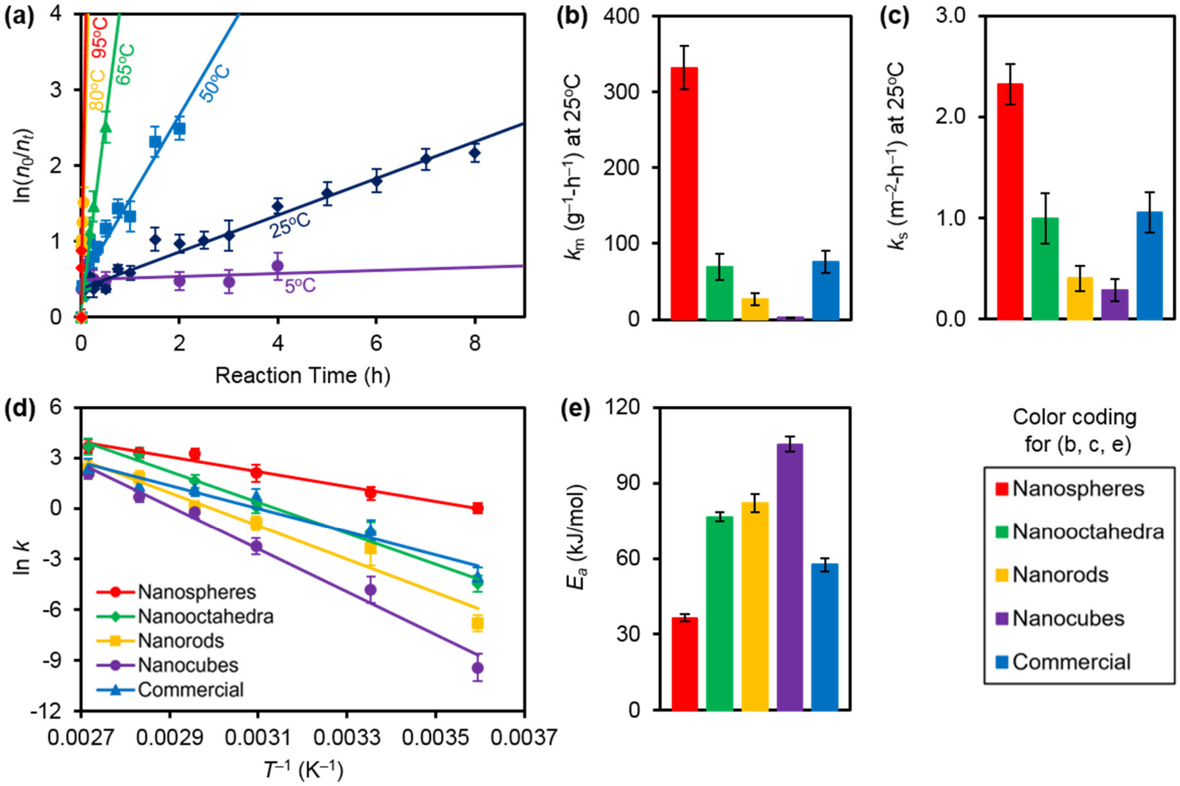

Figure 3. (a) Plots of the reaction rate of dephosphorylation depending on time for CeO_2 nanooctahedra at various temperatures. (b, c) Kinetic rate constants (at 25°C) normalized by mass (k_m) and surface area (k_s) of the CeO_2 nanocrystals. (d) Arrhenius plots showing the dependence of rate constant versus temperature and (e) the derived activation energies for the different types of CeO_2 nanocrystals.

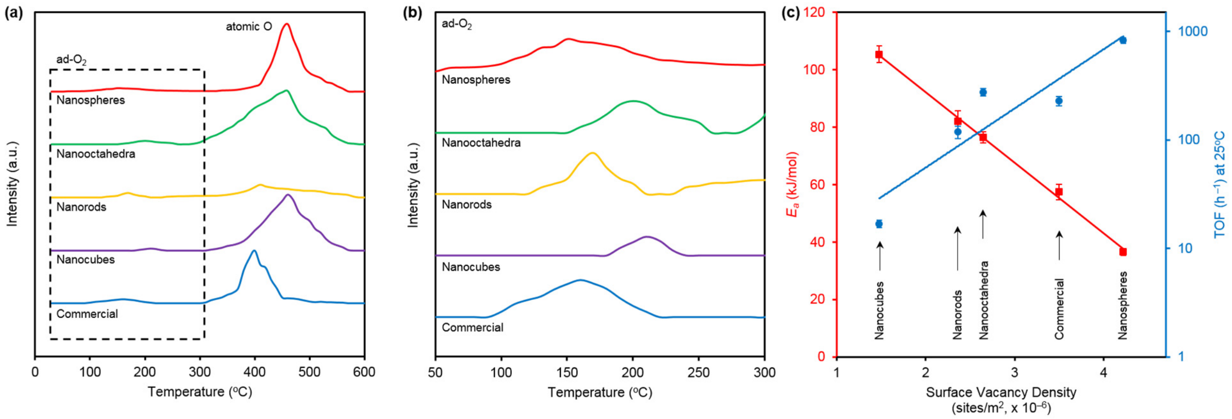

Figure 4. (a) O_2-TPD profiles of the CeO_2 nanocrystals with the region for adsorbed oxygen (ad-O_2) zoomed in (b). (c) Correlations of the activation energy and TOF to the surface density of oxygen vacancies estimated based on the amount of ad-O_2 derived from the O_2-TPD analysis.

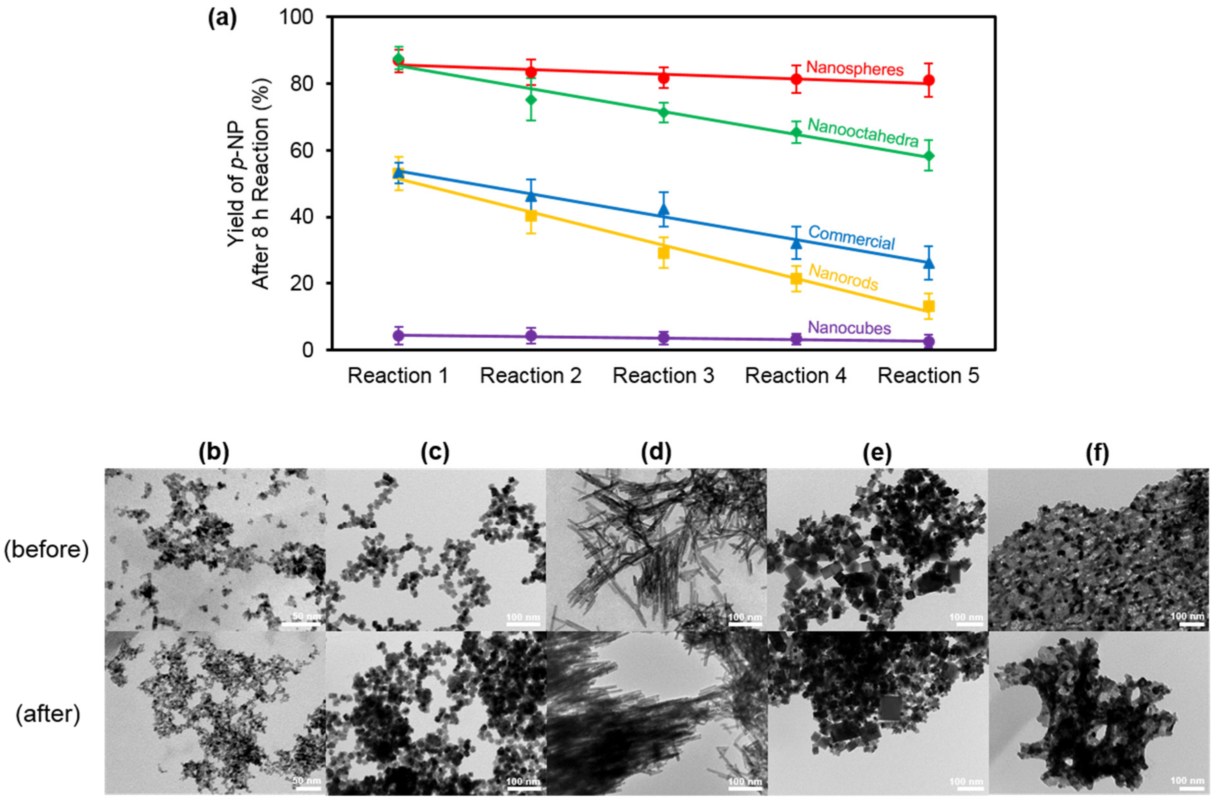

Figure 5. (a) Recyclability of the CeO_2 catalysts measured as *p*-NP yields from successive runs of the dephosphorylation reaction with each run lasting for 8 h. TEM images of the (b) CeO_2 nanospheres, (c) CeO_2 nanooctahedra, (d) CeO_2 nanorods, (e) CeO_2 nanocubes, and (f) commercial CeO_2 nanocatalyst captured before and after recyclability studies.

References

(1) Greenwood, N. N.; Earnshaw, A. *Chemistry of the Elements*. 2nd Ed.; Elsevier: Oxford, 1997.

(2) Black, C. A. *Soil Plant Relationships*. Wiley: New York, 1957.

(3) Buckman, H. O.; Brady, N. C. *The Nature and Properties of Soils*. 6th Ed.; Macmillan: New York. 1960.

(4) Cordell, D.; White, S. *Sustainability* **2011**, *3*, 2027-2049.

(5) Cordell, D.; Schmid-Neset, T.; White, S.; Drangert, J. In *International Conference on Nutrient Recovery from Wastewater Streams*; Ashley, K., Mavinic, D., Koch, F., Eds.; IWA: London, 2009.

(6) Syers, K.; Bekunda, M.; Cordell, D.; Corman, J.; Johnston, J.; Rosemarin, A.; Salcedo, I.; Lougheed, T. In *United Nations Environment Programme Year Book 2011: Emerging Issues in Our Global Environment*; Goverse, T., Bech, S., Eds.; United Nations: New York, 2011.

(7) Tong, J.; Chen, Y. *Environ. Sci. Technol.* **2007**, *41*, 7126-7130.

(8) Battistoni, P.; Fava, G.; Pavan, P.; Muscacco, A.; Cecchi, F. *Wat. Res.* **1997**, *11*, 2925-2929.

(9) Taylor, A. W.; Frazier, A. W.; Gurney, E. L. *Trans. Faraday Soc.* **1963**, *59*, 1580-1584.

(10) Golubev, S. V.; Pokrovsky, O. S.; Savenko, V. S. *J. Cryst. Growth* **2001**, *223*, 550-556.

(11) Taylor, A. W.; Frazier, A. W.; Gurney, E. L. *Trans. Faraday Soc.* **1963**, *59*, 1580-1584.

(12) Hester, R. E.; Harrison, R. M. *Waste as a Resource.* Royal Society of Chemistry: Cambridge, 2013.

(13) Wang, Z.; Lin, Y.; Wu, D.; Kong, H. *Chemosphere* **2016**, *144*, 1290-1298.

(14) Park, E.; Choi, J.; Park, Y.; Park, K. *Toxicology* **2008**, *245*, 90-100.

(15) Asati, A.; Santra, S.; Kaittanis, C.; Perez, J. M. *ACS Nano* **2010**, *4*, 5321-5331.

(16) Celardo, I.; Pedersen, J. Z.; Traversa, E.; Ghibelli, L. *Nanoscale* **2011**, *3*, 1411-1420.

(17) Walkey, C.; Das, S.; Seal, S.; Erlichman, J.; Heckman, K.; Ghibelli, L.; Traversa, E.; McGinnis, J. F.; Self, W. T. *Environ. Sci.: Nano* **2015**, *2*, 33-53.

(18) Janos, P.; Henych, J.; Pelant, O.; Pilarova, V.; Vrtoch, L.; Kormunda, M.; Mazanec, K.; Stengl, V. *J. Hazard Mater.* **2016**, *304*, 259-268.

(19) Janos, P.; Lovaszova, I.; Pfeifer, J.; Ederer, J.; Dosek, M.; Loucka, T.; Henych, J.; Kolska, Z.; Milde, D.; Opletal, T.. *Environ. Sci. Nano* **2016**, *3*, 847-856.

(20) Min, Q.; Li, S.; Chen, X.; Abdel-Halim, E. S.; Jiang, L.; Zhu, J. *ACS Appl. Mater. Interfaces* **2015**, *7*, 9563-9572.

(21) Kuchma, M. H.; Komanski, C. B.; Colon, J.; Teblum, A.; Masunov, A. E.; Alvarado, B.; Babu, S.; Seal, S.; Summy, J.; Baker, C. H. *Nanomed.* **2010**, *6*, 738–744.

(22) Wang, Z.; Bi, W.; Ma, S.; Lv, N.; Zhang, J.; Sun, D.; Ni, J. *Part. Part. Syst. Charact.* **2015**, *32*, 652-660.

(23) Barth, C.; Laffon, C.; Olbrich, R.; Ranguis, A.; Parent, Ph.; Reichling, M. *Sci. Rep.* **2016**, *6*, 21165.

(24) Luches, P.; Pagliuca, F.; Valeri, S. *Phys. Chem. Chem. Phys.* **2014**, *16*, 18848.

(25) Baron, M.; Bondarchuk, O.; Stacchiola, D.; Shaikhutdinov, S.; Freund, H.J. *J. Phys. Chem. C.* **2009**, *113*, 6042-6049.

(26) Beche, E.; Charvin, P.; Perarnau, D.; Abanades, S.; Flamant, G. *Surf. Interface Anal.* **2008**, *40*, 264-267.

(27) Nolan, M.; Parker, S. C.; Watson, G.W. *Surf. Sci.* **2005**, *595*, 223-232.

(28) Mann, A. K. P.; Wu, Z.; Calaza, F. C.; Overbury, S. H. *ACS Catal.* **2014**, *4*, 2437-2448.

(29) Paier, J.; Penschke, C.; Sauer, J. *Chem. Rev.* **2013**, *113*, 3949-3985.

(30) Self, C. H. *J. Immunol. Methods* **1985**, *76*, 389-393.

(31) Deng, S. P.; Tabatabai, M. A. *Biol. Fertil. Soils* **1997**, *24*, 141-146.

(32) Patil, A. J.; Kumar, R. K.; Barron, N. J.: Mann, S. *Chem. Commun.* **2012**, *48*, 7934-7936.

(33) Tan, F.; Zhang, Y.; Wang, J.; Wei, J.; Cai, Y.; Qian, X. *J. Mass Spectrom.* **2008**, *43*, 628-632.

(34) Capdevila-Cortada, M.; Vile, G.; Teschner, D.; Perez-Ramirez, J.; Lopez, N. *Appl. Catal., B* **2016**, *197*, 299-312.

(35) Wu, Z.; Mann, A. K. P.; Li, M.; Overbury, S. H. *J. Phys. Chem. C* **2015**, *119*, 7340-7350.

(36) Wang, L.; Wang, Y.; Zhang, Y.; Yu, Y.; He, H.; Qin, X.; Wang, B. *Catal. Sci. Technol.* **2016**, *6*, 4840-4848.

(37) Ma, C.; Wang, D.; Xue, W.; Dou, B.; Wang, H.; Hao, Z. *Environ. Sci. Technol.* **2011**, *45*, 3628-3634.

(38) Fernandez-Torre, Kosminder, K.; Carrasco, J.; Ganduglia-Pirovano, M. V.; Perez, R. *J. Phys. Chem. C*, **2012**, *116*, 13584-13593.

(39) Wang, G.; Wang, L.; Fei, X.; Zhou, Y.; Sabirianov, R. F.; Mei, W. N.; Cheung, C. L. *Catal. Sci. Technol.* **2013**, *3*, 2602-2609.

(40) Wang, Y.; Wang, F.; Song, Q.; Xin, Q.; Xu, S.; Xu, J. *J. Am. Chem. Soc.* **2013**, *135*, 1506-1515.

(41) Janos, P.; Lovaszova, I.; Pfeifer, J.; Ederer, J.; Dozek, M.; Loucka, T.; Henych, J.; Kolska, Z.; Milde, D.; Opletal, T. *Environ. Sci.: Nano* **2016**, *3*, 847-856.

(42) Zhang, Z.; Glotzer, S. C., *Nano Lett.* **2004**, *4*, 1407-1413.

(43) Damasceno, P. F.; Engel, M.; Glotzer, S. C., *Science* **2012**, *337*, 453-457.

(44) Bishop, K.; Wilmer, K. E.; Soh, S.; Grzybowski, B. A., *Small* **2009**, *5*, 1600–1630.

(45) Ehlerova, J.; Trevani, L.; Sedlbauer, J.; Tremaine, P. *J. Solution Chem.* **2008**, *37*, 857-874.

(46) Murphy, J.; Riley, J. P. *Anal. Chim. Acta* **1962**, *27*, 31-36.

(47) Heinonen, J. K.; Lahti, R. K. *Anal. Biochem.* **1981**, *113*, 313-317.

Table of Contents Graphic